



Pushing the boundaries
of chemistry?
It takes
#HumanChemistry

Make your curiosity and talent as a chemist matter to the world with a specialty chemicals leader. Together, we combine cutting-edge science with engineering expertise to create solutions that answer real-world problems. Find out how our approach to technology creates more opportunities for growth, and see what chemistry can do for you at:

evonik.com/career

 **EVONIK**
Leading Beyond Chemistry

DOI: 10.1002/adma.202108615

Article type: Communication

Anisotropic carrier mobility from 2H WSe₂

By Ping Chen,[#] Jinbo Pan,[#] Wenchao Gao,[#] Bensong Wan, Xianghua Kong, Yang Cheng, Kaihui Liu, Shixuan, Du,^{*} Wei Ji,^{*} Caofeng Pan,^{*} Zhong Lin Wang

Prof. P. Chen, Prof. Z. L. Wang and Prof. C. Pan

Center on Nanoenergy Research, School of Physical Science and Technology, Guangxi University, Nanning 530004, China

Prof. P. Chen, Dr. B. Wan, Prof. Z. L. Wang and Prof. C. Pan

CAS Center for Excellence in Nanoscience, Beijing Key Laboratory of Micro-nano Energy and Sensor, Beijing Institute of Nanoenergy and Nanosystems, Chinese Academy of Sciences, Beijing 100083, China

E-mail: cfpan@binn.cas.cn;

Prof. C. Pan

College of Physics and Optoelectronic Engineering, Shenzhen University, Shenzhen, 518060, China

Prof. Z. L. Wang and Prof. C. Pan

School of Nanoscience and Technology, University of Chinese Academy of Sciences, Beijing 100049, China

[#] These authors contributed equally to this work.

This article has been accepted for publication and undergone full peer review but has not been through the copyediting, typesetting, pagination and proofreading process, which may lead to differences between this version and the [Version of Record](#). Please cite this article as [doi: 10.1002/adma.202108615](https://doi.org/10.1002/adma.202108615).

This article is protected by copyright. All rights reserved.

Prof. Z. L. Wang

School of Materials Science and Engineering, Georgia Institute of Technology, Atlanta, Georgia 30332-0245, United States

Dr. X. Kong

Centre for the Physics of Materials and Department of Physics, McGill University, Montreal QC H3A 2T8, Canada

Y. Cheng, Prof. K. Liu

State Key Laboratory for Mesoscopic Physics, Academy for Advanced Interdisciplinary Studies, School of Physics, Peking University, Beijing 100871, China

Prof. J. Pan, Prof. S. Du

Institute of Physics & University of Chinese Academy of Sciences, Chinese Academy of Sciences, Beijing 100190, China

Email: sxdu@iphy.ac.cn

Prof. W. Ji

Department of Physics and Beijing Key Laboratory of Optoelectronic Functional Materials & Micro-Nano Devices, Renmin University of China, Beijing 100872, China.

Email: wji@ruc.edu.cn

Keywords: anisotropic carrier mobility, intrinsic screening layer, defect scattering, electronic structure, 2H WSe₂

Abstract: Transition metal dichalcogenides (TMDCs) with 2H phase are expected to be the building blocks in next-generation electronics, however, suffered from electrical anisotropy, which is the basics for multi-terminal artificial synaptic devices, digital inverters, and anisotropic memtransistors that are highly desired in neuromorphic computing. Herein, the anisotropic carrier mobility from 2H WSe₂ is reported for the first time, where the anisotropic degree of carrier mobility spans from 0.16 to 0.95 for various WSe₂ field effect transistors under a gate voltage of -60 V. Phonon scattering, impurity ions scattering, and defect scattering are excluded for anisotropic mobility. Intrinsic screening layer is proposed and confirmed by Z-contrast STEM imaging to respond to the electrical anisotropy. Seven types of intrinsic screening layers are created and calculated by density functional theory to evaluate modulated electronic structures, effective masses, and scattering intensities, resulting in anisotropic mobility. The discovery of anisotropic carrier mobility from 2H WSe₂ provides a degree of freedom for adjusting the physical properties of 2H TMDCs and a fertile ground for exploring and integrating the TMDCs electronic transistors with better performance along the direction of high mobility.

Multiterminal synaptic devices based on electrical anisotropy provides a freedom dimension for axon-multi-synapses net-work in brain-like computing,^[1] where two-terminal artificial synapses are proposed first for signal transmission.^[2] However, the two-terminal artificial synapses are suffered from processing signal transmission and learning functions simultaneously. Then, three-terminal artificial synapses have been researched to overcome those problems of two-terminal artificial synapses with the channel materials as synaptic weight.^[3] Three-terminal synaptic transistors have been achieved recently based on various novel materials,^[4] containing SiO₂-based proton conducting electrolytes,^[4a-g] spin-coated organic electrolytes,^[5] and exfoliated two-dimensional (2D) materials.^[1a] The energy dissipation per spike was calculated to be 438 pJ in multiterminal oxide neuro-transistor.^[4g] Multi-gate 2D MoS₂ synaptic transistor presented the energy consumption of single spike event 23.6 pJ.^[6] Organic nanowire synaptic transistor reduced energy consumption per switching event to 10 fJ.^[7] However, three-terminal synaptic devices are essentially the simple counterpart of two-terminal biological synaptic devices, lacking the feasibility to extend neuromorphic computing paradigms beyond vector-matrix multiplication, such as intrinsic electrical anisotropy. Meanwhile, the low energy consumption based on 2D synaptic transistor suggests the superiority and potential application for next-generation computing technologies,^[8] promoting the exploitation of intrinsic electrical anisotropy from 2D materials. Thus, the carrier anisotropy from 2D materials is the hot topics in recent years, where two types can be concluded: semiconductors and semi-metals.

The carrier anisotropy from 2D semiconductors was first discovered from black phosphorus for the light and heavy carrier effective masses from various crystal directions.^[9] Then, the anisotropy of carrier mobility from 2D materials with a puckered crystal structure has been developed, such as

Accepted Article

SnSe,^[10] SnS,^[11] GeSe/GeS.^[12] The different effective masses from armchair and zigzag directions are responded to the electrical anisotropy. Recently, the new multilayer materials fabricated by mechanical stripping, for example Ta₂NiS₅,^[13] GeSe₂,^[14] GaAs₂,^[15] GeP,^[16] and TaIrTe₄,^[17] have presented the carrier mobility anisotropy for the same reasons. However, those 2D semiconductors are suffered from the poor stability for the practical applications.^[18]

The 2D materials with semi-metal property were also exploited, such as GaAs,^[19] ZrTe₅,^[20] ZrB₂,^[21] ReS₂,^[22] ReS_{2(1-x)Se_{2x}},^[23] 1-T' MoS₂.^[24] Excepting from the different effective masses, the path of carrier transport with gate voltage regulation was calculated. Taking ZrB₂ for example, the electrical transport along armchair and zigzag directions is dominated by metallic Zr-Zr bonds under low biases,^[21] while B-B transport channels are opened under high biases. Yet the application is limited by the semi-metal property and instability.

Therefore, the 2D materials with perfect stability and electrical anisotropy have not been achieved. Considering the 2D semiconductor with the perfect stability and suitable preparation process, transition metal dichalcogenides (TMDCs) with 2H phase are the first choice.^[25] But the carrier transport in monolayer TMDCs is isotropic for the same effective mass in different orientations at K and K' valleys.^[26]

Herein, we present the anisotropic carrier mobility in 2H WSe₂, where the degree of mobility anisotropy is spanned from 0.16 to 0.95 with the gate voltage at -60 V. We propose the model of the partially covered 'second' layer WSe₂, called the intrinsic screening layer, to explain the anisotropic carrier mobility, which is confirmed by the experiment results and theoretical calculation. Seven types of intrinsic screening layers and electronic structures are defined and calculated by density

functional theory (DFT) to evaluate the mechanism of electrical anisotropy, containing the clusters of W, Se, and WSe atoms, and the adlayers of W, Se, WSe, and WSe₂. The various scattering intensities, effective masses, and transport pathways, induced by the intrinsic screening layers, response to electrical anisotropy. We believe the anisotropic carrier mobility would find breakthroughs in perspectives of multi-terminal artificial synaptic devices, electronic components, brain-like computing, sensors, and so on.

Six pairs of diagonal electrodes (10 nm Ni/50 nm Au) were prepared on monolayer WSe₂ spaced at the angle of 30° (**Figure 1a**). The atomic force microscope (AFM) image clearly identified the WSe₂ thickness to around 0.7 nm (Figure 1d), confirmed the monolayer structure. The diagonal electrodes marked 0° is presented as reference direction, which was measured first in the experiment. The transfer curves of field effect transistors (FETs) from the angle-resolved diagonal electrodes with the bottom gate voltage are shown in Figure 1b. The drain-source current (I_{ds}) is enhanced with increasing negatively the gate voltage under the drain-source bias V_{ds} at 0.1 V, indicating a *p*-type channel behavior of monolayer WSe₂. On-off current ratio of FET devices from different diagonal electrodes is higher than 5×10^6 . The output current shows a decreased trend from 0° to 60° with decreasing the gate voltage, and then presents an increased trend from 60° to 150°, suggesting the anisotropic carrier transport.

Field effect mobility for angle-resolved diagonal electrodes of the WSe₂ FET devices was calculated using the equation $\mu = [dI_{ds}/dV_{bg}] \times [Ld/(W\varepsilon_0\varepsilon_rV_{ds})]$, where $L = 31.9 \mu\text{m}$ is the channel length, $d = 300 \text{ nm}$ is the SiO₂ thickness, $W = 3.0 \mu\text{m}$ is the channel width, $\varepsilon_0 = 8.854 \times 10^{-12} \text{ C}^2/\text{Nm}^2$ is the vacuum permittivity, $\varepsilon_r = 3.9$ is the relative permittivity of SiO₂. The maximum mobility is $117 \text{ cm}^2/\text{V}\cdot\text{s}$ at 150° and the minimum mobility is $49 \text{ cm}^2/\text{V}\cdot\text{s}$ at 30° with the gate voltage

Accepted Article

at -60 V (Figure 1c), suggesting the anisotropic carrier transport in monolayer WSe₂. For all the FET calculation, mobility is overestimated because the actual channel width is larger than 3 μm (electrodes' width), however, the overestimation for all FETs is the same. And the mechanism of large mobility will be reported in another paper. Then the polar, plotting the dependence of carrier mobility on the angles with the gate voltage at -60 V, was simulated using trigonometric function to illuminate the changed trend clearly (Figure 1e). A sinusoid curve is presented, similar to the anisotropic carrier conductivity in black phosphor.^[9,27] For the purpose to check the credibility of the anisotropic carrier mobility in monolayer WSe₂, multiple FET devices were prepared and measured. We define the degree of polarization/anisotropy $\rho = \frac{\mu_{max} - \mu_{min}}{\mu_{max} + \mu_{min}}$, where μ_{max} is the maximum mobility and μ_{min} is the minimal mobility. The FET devices give the various degree of polarization/anisotropy from 0.16 to 0.95 with the gate voltage at -60 V, declaring the real existence of anisotropic carrier mobility in WSe₂.

In order to understand the microscopic mechanism of anisotropic carrier mobility from monolayer WSe₂, we first study the type of contact between the Ni/Au electrodes and WSe₂, because the barrier height from Schottky contact influences significantly the carrier injection^[28] and the calculated mobility.^[29] All of the output curves from Ni/Au electrodes of the WSe₂ FET devices show the perfect linear features (Figure S1 and S2), indicating the Ohmic contacts between the electrodes and WSe₂. Meanwhile, the contact resistances are calculated to be 12964 Ω (Figure S2d), while total resistances of any WSe₂ FET devices are at least 10⁸ Ω with the gate voltage and drain-source bias at -60 V and 0.1 V, respectively, indicating the channel resistances are the magnitude of 10⁸ Ω. The gap of four order of magnitude between contact resistances and channel resistance

demonstrates the negligible effect of contacts between WSe₂ and Ni/Au electrodes. Thus, the contacts are not the main reason for the anisotropic carrier mobility.

The factors influencing the carrier mobility, phonon scattering, impurity ions scattering, and effective mass are discussed as follows.

Phonon scattering is the main factor affecting the carrier mobility of monolayer TMDCs at room temperature,^[30] which can be reflected from the polarization-resolved Raman scattering. The spectrum from WSe₂ FET devices gives two peaks centered around 249 cm⁻¹ and 260 cm⁻¹ (Figure S3), suggesting the 2H phase of monolayer WSe₂. The Raman peak around 249 cm⁻¹ is ascribed to the out-of-plane mode A_{1g} ,^[31] and the weak peak centered at 260 cm⁻¹ is attributed to E_{2g}^1 mode for the second order peak from the longitudinal acoustic phonons at the M point in the Brillouin zone.^[32] The B_{2g}^1 mode centered on 304 cm⁻¹ is not observed, which is the fingerprint of few-layer WSe₂,^[33] proving the monolayer thickness of WSe₂ FET device again. The angle-resolved polarized Raman scattering from WSe₂ FET device illuminates 60° as the maximum angle (**Figure 2a**), where 0° direction is the reference direction of anisotropic carrier mobility. Thus, 90° is presented between the maximum direction of Raman scattering and anisotropic carrier mobility. For the purpose to verify the phenomenon, lots of devices were fabricated and measured. Various degrees of 30°, 60° and 90° between the maximum direction of Raman scattering and anisotropic carrier mobility are also presented (Figure S4), indicating the irrelevance between phonon scattering and the anisotropic carrier mobility.

Charged ions scattering and defect scattering were discussed because the impurity ions and defects are inevitable in TMDCs for the impure raw materials, ion diffusion from the reaction vessels,

and unbalanced reaction conditions. Those scattering can be reflected from the luminescence spectra for the modulation of crystal field by impurity ions and atomic defect. The luminescence spectrum illustrates a luminescence peak at 776 nm (Figure S3b), agreeing well with the emission from monolayer WSe₂.^[34] The polarization-resolved luminescence from the WSe₂ FET devices provides the similar trend with Raman scattering (Figure 2d and S4), seemingly proving the irrelevance between the crystal field and anisotropic carrier mobility.

Then, Raman mapping and PL mapping of the WSe₂ FET device were measured to study the distribution and uniform of charged ions and atomic defects. The Raman and luminescence mapping are carried out at 249 cm⁻¹ and 776 nm, respectively. The Raman mapping shows almost the same intensity across the whole devices (Figure 2e), while luminescence mapping presents a triangle shape (Figure 2f), where the intensity is lower than other area. The lower luminescence intensity implies a poor crystal structure in the triangle area. The similar phenomena are also discovered in other devices with anisotropic carrier mobility (Figure S5), explaining that the different crystal structures in those monolayer WSe₂ cause the anisotropic carrier mobility.

Atomic defects in WSe₂ were first examined for reduced luminescence intensity with the defects inducing poor crystal structure. Furthermore, the type and distribution of atomic defects could introduce localized mid-gap states and scatter carriers, resulting in the reduced conductivity around line defects.^[35] DFT shows the defects will induce anisotropic conductivity along armchair and zigzag directions when the concentration of point defects is higher than $1.86 \times 10^{12} \text{cm}^{-2}$.^[35] The defect structure was characterized by scanning transmission electron microscope (STEM), where a high-magnification annular dark-field (ADF) imaging was recorded at 200 kV primary voltages. It was difficult for us to find the point defect in our monolayer WSe₂. Only few defects can be found after

searching for a long time (Figure S6 and S8), indicating the low defect concentration in the monolayer WSe₂.

Thinking carefully about the local characterization of STEM, luminescence spectra under low temperature was measured to assess the defect concentration once again. Because the defect luminescence could be appeared at low temperature and the luminescence intensity is positively related with defect concentration.^[36] The luminescence spectra of WSe₂ FET device is shown in Figure S6e. The luminescence spectra give three peaks with decreasing the temperature, which are responded to the neutral excitons, negative trions, and bound excitons at defect sites, respectively.^[37] The defect connected luminescence was first detected at 37 K and then enhanced with decreasing the temperature. It's reported that the defect luminescence appears at 77 K when the defect concentration is $6 \times 10^{11} \text{cm}^{-2}$,^[38] and the luminescence intensity should increase with increasing the defect concentration.^[36] Therefore, the defect concentration in our WSe₂ FET device is much lower than $6 \times 10^{11} \text{cm}^{-2}$ and cannot induce the anisotropic carrier mobility.

During the process of searching defects, a 'galaxy' was in sight and attracted our attentions (Figure S7a). When enlarged the galaxy, lots of 'stars' come into view (Figure S7). That's interesting. Because the atoms should be 'glowed' uniformly with the perfect atom structures of 2H WSe₂, while the bright stars with unevenly distribution imply a new atom structure. Thus, the atom structure was analyzed rigorously and carefully. Parts of W atoms are superimposed by another W atom and form the brightest stars. Some of Se atoms are covered by two Se atoms and show the brighter stars. Also, lots of Se atoms are grown by another Se atom and present the bright stars. And other atoms in monolayer WSe₂ give the normal brightness (**Figure 3**). When the additional atoms come together, the isolated islands are formed, which is like the 'second' layer WSe₂. Thus, we call it intrinsic

screening layer. The intrinsic screening layers are arranged linearly and formed into a galaxy. We speculate that the intrinsic screening layer might be the crystal nuclei of the second layer WSe_2 , because the spiral-shaped layer is grown on the monolayer WSe_2 when extending reaction time (Figure S7).

The intrinsic screening layer could couple with monolayer WSe_2 and the interlayer interaction will modulate the electronic structure of monolayer WSe_2 . Meanwhile, the analogous bilayer structure might lead to the conversion from direct bandgap to indirect bandgap, resulting in the lower luminescence intensity, as shown in Figure 2f.

In order to confirm the proposed mechanism of intrinsic screening layer, seven types of intrinsic screening layers and electronic structures are established and calculated by DFT (Figure 4b-i), the calculation details can be found in *Experimental Section*. The intrinsic screening layers with adsorbed cluster, especially Se atoms, would induce defect scattering and reduce electrical conductivity, while not seriously affect effective mass of monolayer WSe_2 (Figure 4b-d). The adlayers of Se and W atoms could make the WSe_2 become metallic and enhance the electrical conductivity largely (Figure 4e-f). Meanwhile, the adlayers of WSe and WSe_2 atoms could affect the effective masses and electrical conductivity of WSe_2 obviously (Figure 4g-h). Thus, the different kinds of intrinsic screening layers can induce electrical anisotropy of WSe_2 .

Furthermore, to achieve the consistent and robust anisotropic mobility, and understand the link between orientation of anisotropic mobility and intrinsic screening layer. We chose the 1D adlayer of WSe_2 to calculate the conductivity and verify by experiment results, because the 1D ribbon WSe_2 is a common phenomenon during the CVD synthesis for spiral growth of multilayer TMDCs.^[39] The

Accepted Article

electronic structure presents that the effective mass of WSe₂ is not modulated obviously (Figure 4i), while the electrical conductivity along the 1D ribbon direction is enhanced for the additional conductive pathway provided by ribbon layer. The experiment results are agreed well with the DFT calculation, where the conductive ability along 1D ribbon direction shows 3-10 times that of the vertical direction (Figure S9), presenting 0.45-0.95 of the anisotropic degree of carrier mobility. Besides, the electrical anisotropy from 2H MoSe₂ is also presented with 1D ribbon MoSe₂, confirmed the generality of modulated electrical anisotropy by intrinsic screening layer again (Figure S9). Therefore, the consistent and robust anisotropic mobility is achieved, accompanying with the established link between the orientation anisotropic mobility and 1D ribbon direction.

To support the mechanism of the intrinsic screening layer connected the anisotropic scattering, effective mass, and carrier mobility, gate voltage modulated degree of polarization/anisotropy was analyzed. The degree of polarization/anisotropy is reduced with increasing the gate voltage negatively (**Figure 5**), which can be explained from the screening effect. Carrier density (ρ) from WSe₂ increases with increasing the gate voltage negatively ($\rho \propto V_g - V_t$, where V_t is threshold voltage),^[40] causing the enhanced screening ability of carriers to external Coulomb potential,^[41] the reduced scattering of polarized optical phonon scattering from WSe₂ surface,^[42] and the weakening effect from the intrinsic screening layer. Therefore, the electrical behaviors of WSe₂ FET devices are trended to present the performance of monolayer WSe₂, which is electrical isotropic. And the degree of polarization/anisotropy is reduced with increasing the gate voltages negatively, conformed the microscopic mechanism again. Furthermore, we can expect the modulated anisotropic ratio from other 2D materials, also those with intrinsic electrical anisotropy, such as SnS, SnSe, because various

mobilities and effective masses from monolayer, bilayer, or multilayer materials construct the basis of intrinsic screening layer regulating electrical anisotropy.^[43]

In summary, we have introduced the anisotropic carrier mobility from 2H WSe₂ for the first time and proposed the mechanism of intrinsic screening layers modulating electrical anisotropy, excluding phonon scattering, impurity ions scattering, and defect scattering. The clusters of W, Se, and WSe atoms could induce defect scattering to reduce electrical conductivity. The adlayers of W and Se will make WSe₂ become metallic and enhance the electrical conductivity. And the adlayers of WSe and WSe₂ would affect the effective mass and electrical conductivity simultaneously. Besides, the consistent anisotropy mobility has been achieved with 1D WSe₂ ribbon, which are verified by theoretical calculations and experimental results. The excellent photo-electrical performances and perfect stability of 2H WSe₂ lay the foundation for microelectronics applications with the channel length less than 10 nm.^[44] The discovered anisotropy of carrier mobility from 2H WSe₂ provides the new idea for designing and fabricating new electronic devices, such as high-speed electronics and radio frequency nanoelectronics. The electrical anisotropy also offers the path to multi-terminal artificial synaptic devices in neuromorphic computing.

Experimental Section

Synthesis of WSe₂: The monolayer WSe₂ was grown by physical vapor deposition.^[25] WSe₂ powder (99.9%, Alfa) was used as the raw material. 1 g WSe₂ powder was supported by quartz boat and placed at the center of furnace in 1-inch quartz tube. The substrate of 300 nm SiO₂/Si was put at

downstream end of the furnace. The tube was heated up to 1180 °C and kept 5 min under ambient pressure with the Ar flow 80 sccm. Then the furnace was cooled down naturally.

FET fabrication: The FET devices were fabricated by electron-beam lithography (EBL) and thermal evaporation. Monolayer WSe₂, supported by 300 nm SiO₂/Si substrate, was spin-coated by poly (methyl methacrylate) (PMMA) with 4000 rpm for 60 s, followed by heating at 150 °C for 5 min. EBL was used to open electrode patterns and Ni/Au (10/50 nm) was deposited by thermal evaporation. The sample was immersed into acetone to remove the residual PMMA.

Transfer monolayer WSe₂ to TEM grid: PMMA was spin-coated on monolayer WSe₂ supported by 300 nm SiO₂/Si substrate, followed by heating at 120 °C for 3 min. The edge of PMMA was removed by a blade and immersed into NaOH solution (1 mol/L). After dropped from the substrate, PMMA was transfer onto a TEM grid and washed by water for several times. The target sample on TEM grid was immersed into acetone for 10 minutes to remove PMMA and washed by acetone for several time.

Electrical and optical characterization: The electrical properties of WSe₂ FET devices were measured by a Keithley 4200-CSC parameter analyzers. Optical properties of WSe₂ FET devices in room temperature were carried out on an HR 800, HORIBA Jobin Yvon spectrometer with an excited source at 532 nm. Optical properties of WSe₂ FET devices at low temperature were carried by Princeton Instruments Acton SpectraPro SP-2500 spectrometer equipped with a Montana Instruments cryostat excited by 532 nm.

AFM and STEM Z-contrast analysis: AFM image of monolayer WSe₂ FET devices was obtained on SPM9700 microscopy with the operated voltage at 200 kV. STEM imaging was performed on a spherical aberration-corrected FEI-Titan Cubed Themis G2 300 operated at 200 kV.

DFT calculations: DFT calculations were performed using the projector-augmented wave (PAW) pseudopotentials in conjunction with the Perdew-Burke-Ernzerhof (PBE) exchange-correlation functional as implemented in Vienna Ab-initio Simulation Package (VASP). The energy cutoff of plane-wave was set to 400 eV. The thicknesses of vacuum length were larger than 15 Å. 4 × 4 WSe₂ supercells were used as the simulate the adlayers on WSe₂ surfaces. We employed a nonlocal correction function vdW-DF (optB86b)^[45] to consider the van der Waals interactions between adsorbates and WSe₂ monolayers. All the structural models were relaxed until the force on each atom is less than 0.02 eVÅ⁻¹, and the break condition of the electronic self-consistent loop was set at 1 × 10⁻⁶ eV. K-meshes of 3 × 3 × 1 were adopted to sample the Brillouin zones of the conventional unit cell for structural properties. The electronic band structures were all unfolded to the primitive cells using the VaspBandUnfolding code.

Supporting Information

Supporting Information is available from the Wiley Online Library or from the author.

Acknowledgements

The authors express thanks for the support from National Natural Science Foundation of China (No. 11704081, 52125205, U20A20166, 61805015 and 61804011), Guangxi Natural Science Foundation (No. 2017GXNSFBA198229, 2020GXNSFAA297182), Natural Science Foundation of Beijing Municipality (Z180011), Shenzhen Science and Technology Program (Grant No. KQTD20170810105439418) and the Fundamental Research Funds for the Central Universities.

Received: ((will be filled in by the editorial staff))

Revised: ((will be filled in by the editorial staff))

Published online: ((will be filled in by the editorial staff))

References

- [1] a) V. K. Sangwan, H. Lee, H. Bergeron, I. Balla, M. E. Beck, K. Chen, M. C. Hersam, *Nature* **2018**, *554*, 500; b) J. Guo, Y. Liu, F. Zhou, F. Li, Y. Li, F. Huang, *Adv. Funct. Mater.* **2021**, *31*, 2102015; c) X. Feng, S. Li, S. L. Wong, S. Tong, L. Chen, P. Zhang, L. Wang, X. Fong, D. Chi, K. Ang, *ACS Nano* **2021**, *15*, 1764.

- [2] A. Stoddart, *Nat. Rev. Mater.* **2018**, *3*, 18014.
- [3] Q. Xia, J. J. Yang, *Nat. Mater.* **2019**, *18*, 309.
- [4] a) S. Kim, B. Choi, M. Lim, J. Yoon, H. D. Kim, S. J. Choi, *ACS Nano* **2017**, *11*, 2814; b) C. Wan, G. Chen, Y. Fu, M. Wang, N. Matsuhisa, S. Pan, L. Pan, H. Yang, Q. Wan, L. Wan, L. Zhu, X. Chen, *Adv. Mater.* **2018**, *30*, 1801291; c) Y. Yang, Y. He, S. Nie, Y. Shi, Q. Wan, *Device Lett.* **2018**, *39*, 897; d) W. Huh, S. Jang, J. Y. Lee, D. Lee, D. Lee, J. M. Lee, H. Park, J. C. Kim, H. Y. Jeong, G. Wang, C. Lee, *Adv. Mater.* **2018**, *30*, 1801447; e) L. Q. Zhu, C. J. Wan, L. Q. Guo, Y. Shi, Q. Wan, *Nat. Commun.* **2014**, *5*, 3158; f) L. Wang, W. Liao, S. L. Wong, Z. G. Yu, S. Li, Y. Lim, X. Feng, W. C. Tan, X. Huang, L. Chen, L. Liu, J. Chen, X. Gong, C. Zhu, X. Liu, Y. Zhang, D. Chi, K. Ang, *Adv. Funct. Mater.* **2019**, *29*, 1901106; g) C. J. Wan, L. Q. Zhu, Y. H. Liu, P. Feng, Z. P. Liu, H. L. Cao, P. Xiao, Y. Shi, Q. Wan, *Adv. Mater.* **2016**, *28*, 3557; h) K. Zhou, W. Xu, Y. Yu, W. Zhai, Z. Yuan, K. Dai, G. Zheng, L. Mi, C. Pan, C. Liu, C. Shen, *Small* **2021**, *17*, 2100542; i) J. Sun, Q. Hua, M. Zhao, L. Dong, Y. Chang, W. Wu, J. Li, Q. Chen, J. Xi, W. Hu, C. Pan, C. Shan, *Adv. Mater. Technol.* **2021**, 2100229; j) J. Sun, Y. Chang, L. Dong, K. Zhang, Q. Hua, J. Zang, Q. Chen, Y. Shang, C. Pan, C. Shan, *Nano Energy* **2021**, *86*, 106077; k) H. Liu, X. Chen, Y. Zheng, D. Zhang, Y. Zhao, C. Wang, C. Pan, C. Liu, C. Shen, *Adv. Funct. Mater.* **2021**, *31*, 2008006; l) K. Zhou, Y. Zhao, X. Sun, Z. Yuan, G. Zheng, K. Dai, L. Mi, C. Pan, C. Liu, C. Shen, *Nano energy* **2020**, *70*, 104546; m) C. Wang, C. Pan, Z. L. Wang, *ACS Nano* **2019**, *13*, 12287; n) H. Liu, Q. Hua, R. Yu, Y. Yang, T. Zhang, Y. Zhang, C. Pan, *Adv. Funct. Mater.* **2016**, *26*, 5307.
- [5] G. G. Turrigiano, S. B. Nelson, *Nat. Rev. Neurosci.* **2004**, *5*, 97.

- [6] J. Jiang, J. Guo, X. Wan, Y. Yang, H. Xie, D. Niu, J. Yang, J. He, Y. Gao, Q. Wan, *Small* **2017**, *13*, 1700933.
- [7] W. Xu, S. Min, H. Hwang, T. Lee, *Sci. Adv.* **2016**, *2*, e1501326.
- [8] C. Liu, H. Chen, S. Wang, Q. Liu, Y. Jiang, D. W. Zhang, M. Liu, P. Zhou, *Nat. Nanotechnol.* **2020**, *15*, 545.
- [9] F. Xia, H. Wang, Y. Jia, *Nat. Commun.* **2014**, *5*, 4458.
- [10] X. Xu, Q. Song, H. Wang, P. Li, K. Zhang, Y. Wang, K. Yuan, Z. Yang, Y. Ye, L. Dai, *ACS Appl. Mater. Interfaces* **2017**, *9*, 12601.
- [11] Z. Tian, C. Guo, M. Zhao, R. Li, J. Xue, *ACS Nano* **2017**, *11*, 2219.
- [12] Z. Li, X. Liu, X. Wang, Y. Yang, S. Liu, W. Shi, Y. Li, X. Xing, D. Xue, J. Hu, *Phys. Chem. Chem. Phys.* **2020**, *22*, 914.
- [13] L. Li, P. Gong, W. Wang, B. Deng, L. Pi, J. Yu, X. Zhou, X. Shi, H. Li, T. Zhai, *ACS Nano* **2017**, *11*, 10264.
- [14] Y. Yang, S. Liu, W. Yang, Z. Li, Y. Wang, X. Wang, S. Zhang, Y. Zhang, M. Long, G. Zhang, D. Xue, J. Hu, L. Wan, *J. Am. Chem. Soc.* **2018**, *140*, 4150.
- [15] L. Li, P. Gong, D. Sheng, S. Wang, W. Wang, X. Zhu, X. Shi, F. Wang, W. Han, S. Yang, K. Liu, H. Li, T. Zhai, *Adv. Mater.* **2018**, *30*, 1804541.
- [16] L. Li, W. Wang, P. Gong, X. Zhu, B. Deng, X. Shi, G. Gao, H. Li, T. Zhai, *Adv. Mater.* **2018**, *30*, 1706771.
- [17] J. Lai, Y. Liu, J. Ma, X. Zhuo, Y. Peng, W. Lu, Z. Liu, J. Chen, D. Sun, *ACS Nano* **2018**, *12*, 4055.

- [18] Y. Huang, J. Qiao, K. He, S. Bliznakov, E. Sutter, X. Chen, D. Luo, F. Meng, D. Su, J. Decker, W. Ji, R. S. Ruoff, P. Sutter, *Chem. Mater.* **2016**, *28*, 8330.
- [19] S. Yang, Y. Yang, M. Wu, C. Hu, W. Shen, Y. Gong, L. Huang, C. Jiang, Y. Zhang, P. M. Ajayan, *Adv. Funct. Mater.* **2018**, *28*, 1707379.
- [20] G. Qiu, Y. Du, A. Charnas, H. Zhou, S. Jin, Z. Luo, D. Y. Zemlyanov, X. Xu, G. J. Cheng, P. D. Ye, *Nano Lett.* **2016**, *16*, 7364.
- [21] Y. An, J. Jiao, Y. Hou, H. Wang, R. Wu, C. Liu, X. Chen, T. W. K. Wang, *J. Phys. Cond. Matter* **2018**, *31*, 065301.
- [22] a) Y. Lin, H. Komsa, C. Yeh, T. Björkman, Z. Liang, C. Huang, P. Chiu, A. V. Krasheninnikov, K. Suenaga, *ACS Nano* **2015**, *9*, 11249; b) E. Liu, Y. Fu, Y. Wang, Y. Feng, H. Liu, X. Wan, W. Zhou, B. Wang, L. Shao, C. Ho, Y. Huang, Z. Cao, L. Wang, A. Li, J. Zeng, F. Song, X. Wang, Y. Shi, H. Yuan, H. Y. Hwang, Y. Cui, F. Miao, D. Xing, *Nat. Commun.* **2015**, *6*, 6991.
- [23] W. Wen, Y. Zhu, X. Liu, H. Hsu, Z. Fei, Y. Chen, X. Wang, M. Zhang, K. Lin, F. Huang, Y. Wang, Y. Huang, C. Ho, P. Tan, C. Jin, L. Xie, *Small* **2017**, *13*, 1603788.
- [24] G. Nam, Q. He, X. Wang, Y. Yu, J. Chen, K. Zhang, Z. Yang, D. Hu, Z. Lai, B. Li, Q. Xiong, Q. Zhang, L. Gu, H. Zhang, *Adv. Mater.* **2019**, *31*, 1807764.
- [25] a) S. Manzeli, D. Ovchinnikov, D. Pasquier, O. V. Yazyev, A. Kis, *Nat. Rev. Mater.* **2017**, *2*, 17033; b) Z. Zhang, P. Chen, X. Duan, K. Zang, J. Luo, X. Duan, *Science* **2017**, *357*, 788.
- [26] J. R. Schaibley, H. Yu, G. Clark, P. Rivera, J. S. Ross, K. L. Seyler, W. Yao, X. Xu, *Nat. Rev. Mater.* **2016**, *1*, 16055.

- [27] B. Wan, S. Guo, J. Sun, Y. Zhang, Y. Wang, C. Pan, J. Zhang, *Sci. Bull.* **2019**, *64*, 254.
- [28] a) R. Yu, S. Niu, C. Pan, Z. L. Wang, *Nano Energy* **2015**, *14*, 312; b) Y. Liu, R. Bao, J. Tao, J. Li, M. Dong, C. Pan, *Sci. Bull.* **2020**, *65*, 70; c) C. Pan, L. Dong, G. Zhu, S. Niu, R. Yu, Q. Yang, Y. Liu, Z. L. Wang, *Nat. Photonics* **2013**, *7*, 752; d) C. Pan, J. Zhai, Z. L. Wang, *Chem. Rev.* **2019**, *119*, 9303; e) Q. Hua, J. Sun, H. Liu, R. Bao, R. Yu, J. Zhai, C. Pan, Z. L. Pan, *Nat. Commun.* **2018**, *9*, 244; f) F. Gao, H. Yang, P. A. Hu, *Small methods* **2018**, *2*, 1700384; g) Z. Li, D. Li, H. Wang, P. Chen, L. Pi, X. Zhou, T. Zhai, *Small methods* **2021**, *5*, 2100567.
- [29] a) J. Chen, P. M. Odenthal, A. G. Swartz, G. C. Floyd, Hua Wen, K. Y. Luo, R. K. Kawakami, *Nano Lett.* **2013**, *7*, 3106; b) J. Liu, Z. Zhang, S. Qiao, G. Fu, S. Wang, C. Pan, *Sci. Bull.* **2020**, *65*, 477.
- [30] B. R. Carvalho, Y. Wang, S. Mignuzzi, D. Roy, M. Terrones, C. Fantini, V. H. Crespi, L. M. Malard, M. A. Pimenta, *Nat. Commun.* **2017**, *8*, 14670.
- [31] E. Corro, H. Terrones, A. Elias, C. Fantini, S. Feng, M. A. Nguyen, T. E. Mallouk, M. Terrones, *ACS Nano* **2014**, *8*, 9629.
- [32] E. Corro, A. Betello-Méndez, Y. Gillet, A. L. Elias, H. Terrones, S. Feng, C. Fantini, D. Rhodes, N. Pradhan, L. Balicas, X. Gonze, J. C. Charlier, M. Terrones, M. A. Pimenta, *Nano Lett.* **2016**, *16*, 2363.
- [33] P. Tonndorf, R. Schmidt, P. Böttger, X. Zhang, J. Börner, A. Liebig, M. Albrecht, C. Kloc, O. Gordan, D. R. T. Zahn, S. M. Vasconcellos, R. Bratschitsch, *Opt. Express* **2013**, *21*, 4908.

- [34]a) K. Park, O. Khatib, V. Kravtsov, G. Clark, X. Xu, M. B. Raschke, *Nano Lett.* **2016**, 16, 2621; b) Z. Wei, B. Li, C. Xia, Y. Cui, J. He, J. B. Xia, J. Lim *Small methods* **2018**, 2, 1800094.
- [35]M. Ghorbani-Asl, A. N. Enyashin, A. Kuc, G. Seifert, T. Heine, *Phys. Rev. B* **2013**, 88, 245440.
- [36]Z. Wu, Z. Luo, Y. Shen, W. Zhao, W. Wang, H. Nan, X. Guo, L. Sun, X. Wang, Y. You, Z. Ni, *Nano Res.* **2016**, 9, 3622.
- [37]Y. You, X. Zhang, T. C. Berkelbach, M. S. Hybertsen, D. R. Reichman, T. F. Heinz, *Nat. Phys.* **2015**, 11, 477.
- [38]S. Tongay, J. Suh, C. Ataca, W. Fan, A. Luce, J. S. Kang, J. Liu, C. Ko, R. Raghunathanan, J. Zhou, F. Ogletree, J. Li, J. C. Grossman, J. Wu, *Sci. Rep.* **2013**, 3, 2657.
- [39]X. Fan, Y. Zhao, W. Zheng, H. Li, X. Wu, X. Hu, X. Zhang, X. Zhu, Q. Zhang, X. Wang, B. Yang, J. Chen, S. Jin, A. Pan, *Nano Lett.* **2018**, 18, 3885.
- [40]S. Li, K. Wakabayashi, Y. Xu, S. Nakaharai, K. Komatsu, W. Li, Y. Lin, *Nano Lett.* **2013**, 13, 3546.
- [41]X. Cui, G. Lee, Y. D. Kim, G. Arefe, P. Y. Huang, C. Lee, D. A. Chenet, X. Zhang, L. Wang, F. Ye, F. Pizzoczero, B. S. Jessen, K. Watanabe, T. Taniguchi, D. A. Muller, T. Low, P. Kim, J. Hone, *Nat. Nanotech.* **2015**, 10, 534.
- [42]Z. Yu, Z. Ong, S. Li, J. Xu, G. Zhang, Y. Zhang, Y. Shi, X. Wang, *Adv. Funct. Mater.* **2017**, 27, 1604093.

[43] Y. Li, M. Wu, D. K. Song, T. Ding, F. Liu, J. Li, H. Zhang, H. Xie, *ACS Appl. Energy Mater.* **2020**, *3*, 6946.

[44] A. Nourbakhsh, A. Zubair, R. N. Sajjad, A. Tavakkoli, W. Chen, S. Fang, X. Ling, J. Kong, M. S. Dresselhaus, E. Kaxiras, K. K. Berggren, *Nano Lett.* **2016**, *16*, 7798.

[45] J. Klimeš, D. R. Bowler, A. Michaelides, *Phys. Rev. B* **2011**, *83*, 195131.

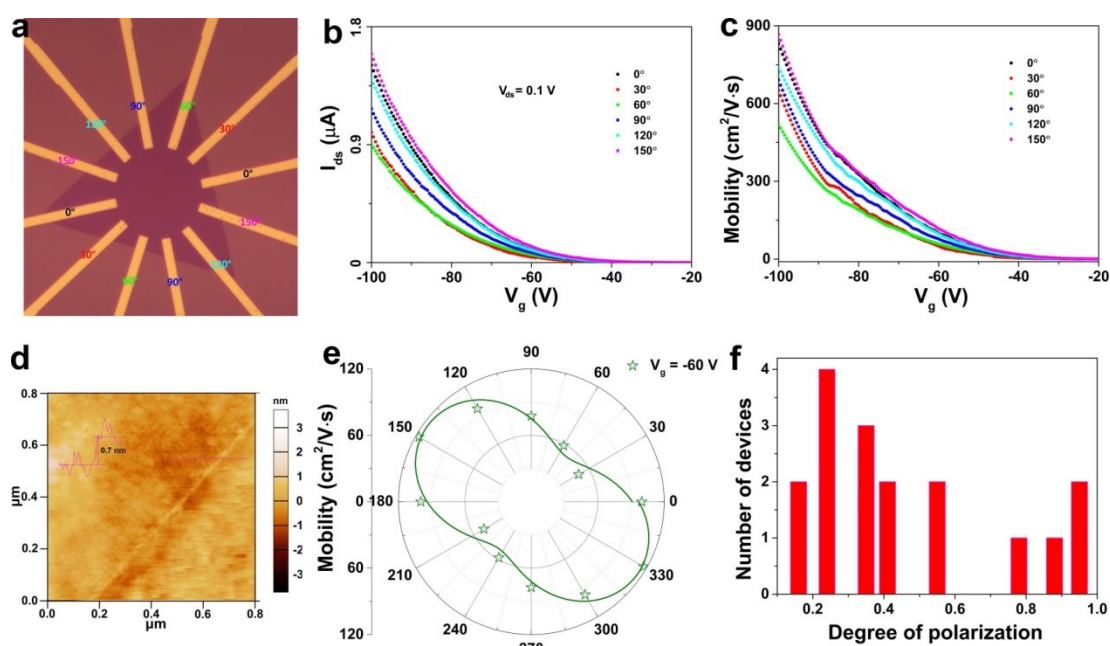


Figure 1. a) Optical image of monolayer WSe₂ FET devices. b) Transfer curves for angle-resolved diagonal electrodes of the WSe₂ FET devices. c) Field effect mobility for angle-resolved diagonal electrodes of the WSe₂ FET devices. d) AFM micrograph of the WSe₂ FET devices. e) Dependence of carrier mobility on the electrodes' angle with the gate voltage at -60 V. f) Histogram of anisotropic degree for carrier mobility from the prepared WSe₂ FETs.

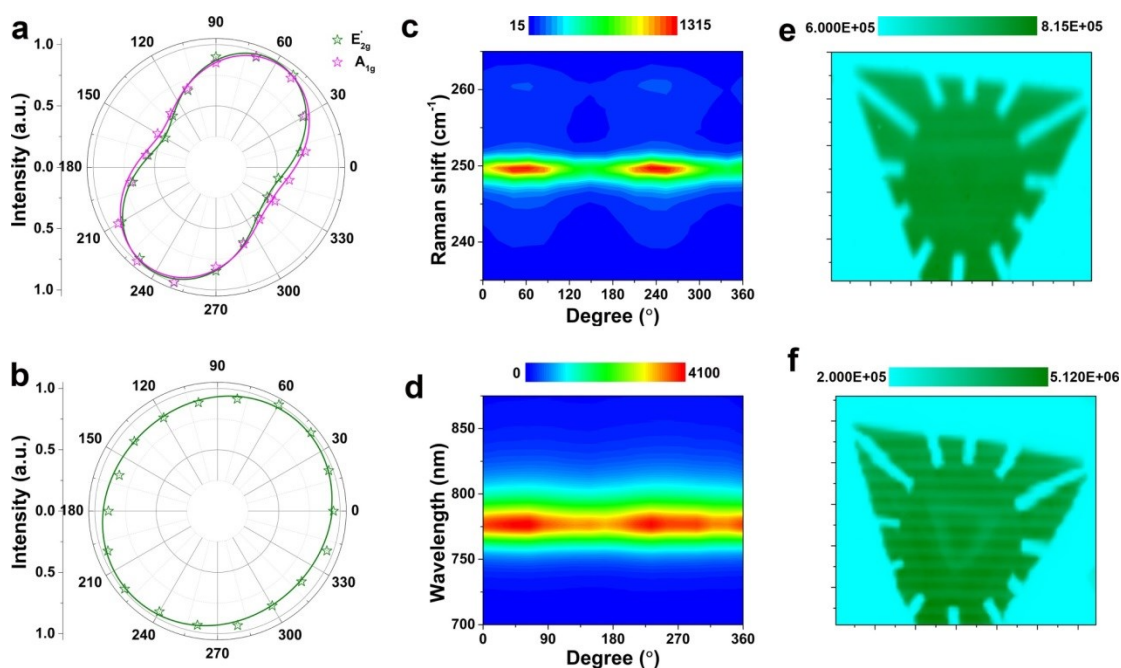


Figure 2. a-b) Polar plots of angle-resolved polarized Raman scattering intensity (a) and photoluminescence intensity (b) from the WSe₂ FET device, respectively. c-d) Dependence of Raman (c) and photoluminescence (d) spectra from the WSe₂ FET device on the polarized angle of excited laser. e-f) Raman (e) and photoluminescence (f) mapping from the WSe₂ FET device. The Raman and luminescence mapping are carried out at 249 cm⁻¹ and the 776 nm, respectively.

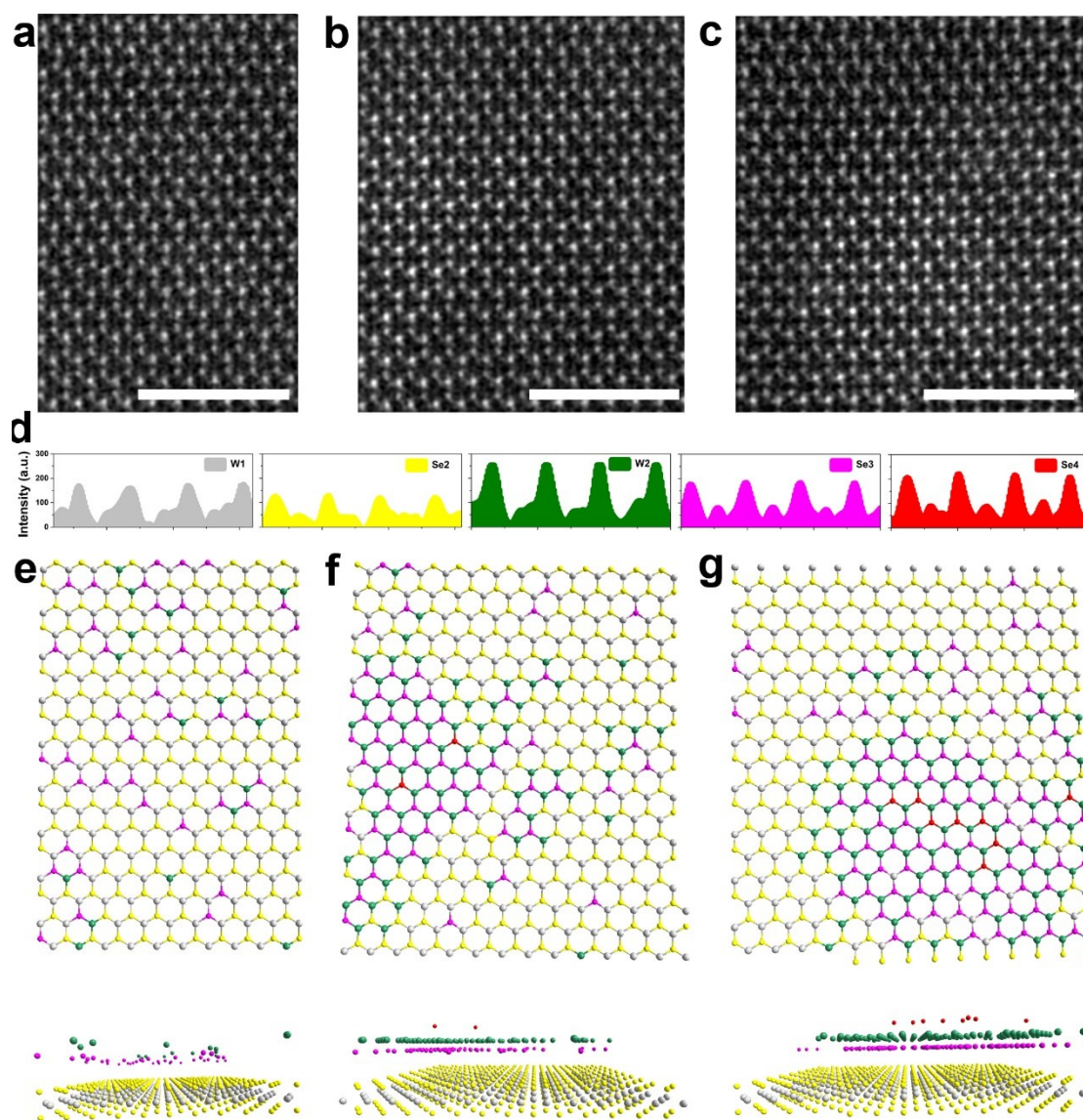


Figure 3. a-c) Atomic resolution Z-contrast images of monolayer WSe₂. d) Intensity profiles of different atom clusters. e-g) The atomic structure determined by the histogram analysis corresponding to images a (e), b (f), and c (g), respectively.

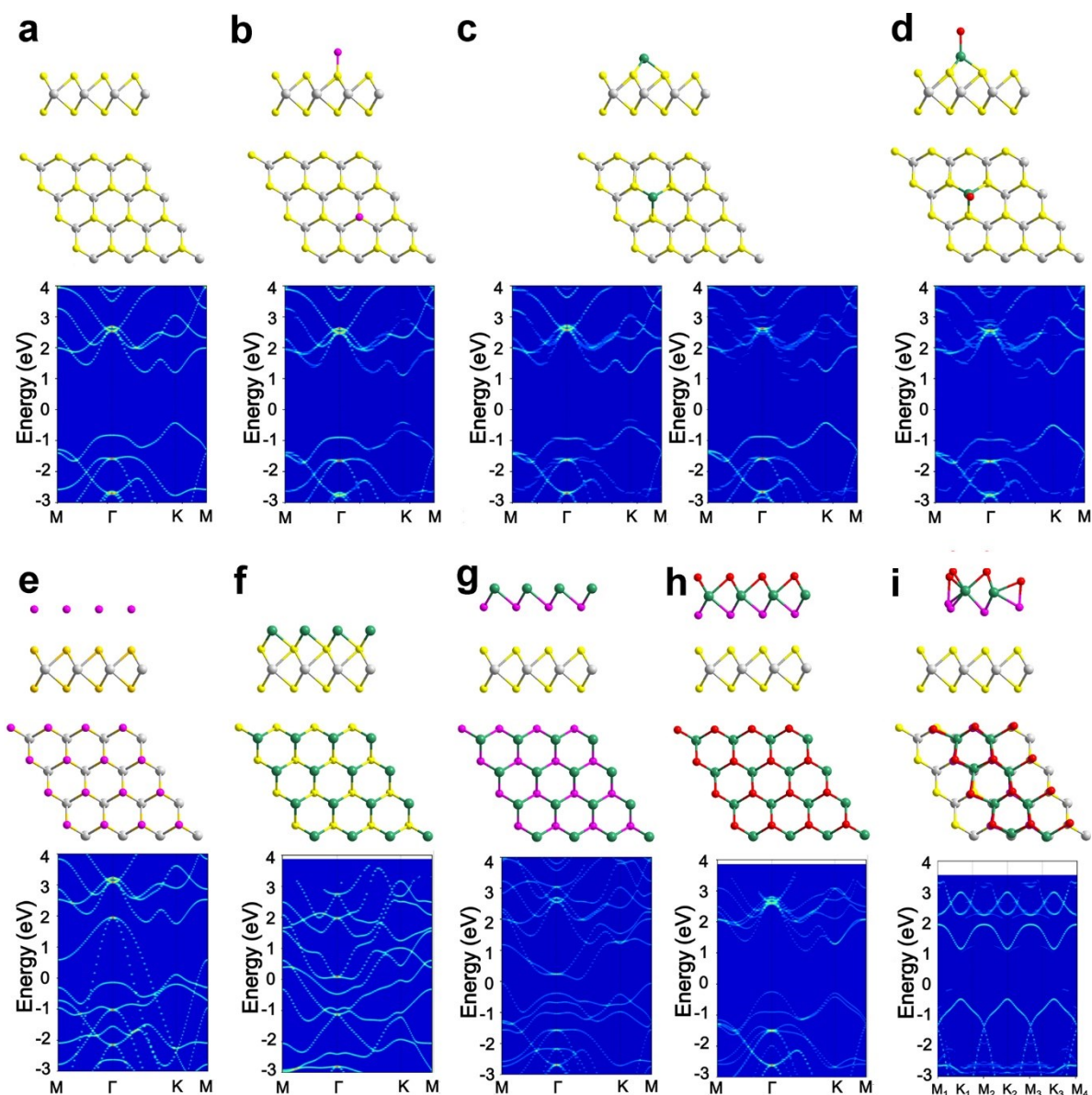


Figure 4. a-d) Crystal structure and electronic structure from monolayer WSe_2 (a), with absorbed cluster Se (b), absorbed cluster W atoms (c), absorbed cluster of W and Se atoms (d), where electronic structures with spin up band (left) and spin down band (right) in c. e-f) Crystal structure and electronic structure from monolayer WSe_2 with adlayers of Se (e) and W (f) atoms, respectively. g) Crystal structure and electronic structure from monolayer WSe_2 with the adlayers of W and Se

atoms. h) Crystal structure and electronic structure from bilayer WSe₂ with AA stacking. i) Crystal structure and electronic structure from monolayer WSe₂ with adlayer of 1D WSe₂ ribbon.

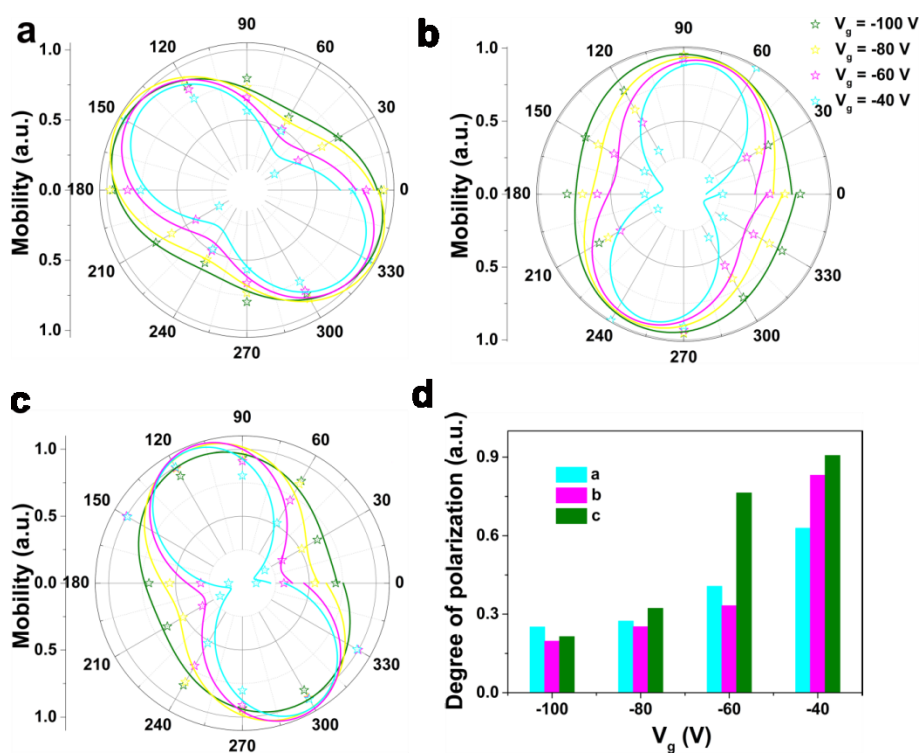


Figure 5. a-c) Polar plots of angle-resolved carrier mobility for three WSe₂ FET devices with the gate voltage at -100 V, -80 V, -60 V, and -40 V. d) Histogram of anisotropic degree of carrier mobility from the three WSe₂ FET under different gate voltages.

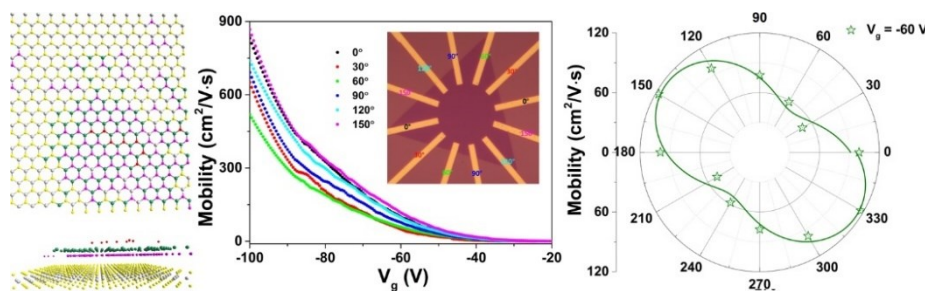
Table of Contents entry

Anisotropic carrier mobility is realized in 2H WSe₂. Intrinsic screening layer is responded to the electrical anisotropy, which is confirmed by theoretical calculations and experimental results, excluding phonon scattering, impurity ions scattering, and defect scattering. The electrical anisotropy provides a degree of freedom for adjusting the physical properties and an essential step for exploring and integrating TMDCs transistors in multi-terminal artificial synaptic devices.

Keywords: *anisotropic carrier mobility, intrinsic screening layer, defect scattering, electronic structure, 2H WSe₂*

Anisotropic carrier mobility from 2H WSe₂

By Ping Chen,[#] Jinbo Pan,[#] Wenchao Gao,[#] Bensong Wan, Xianghua Kong, Yang Cheng, Kaihui Liu, Shixuan, Du,^{*} Wei Ji,^{*} Caofeng Pan,^{*} Zhong Lin Wang



[#] These authors contributed equally to this work.